Carbon Cycling and Habitability of Massive Earth-like Exoplanets

Amanda Kruijver[1,3] , Dennis Höning[1,2,3] , and Wim van Westrenen[1]
[1] Department of Earth Sciences, Vrije Universiteit Amsterdam, The Netherlands
[2] Origins Center, The Netherlands

Abstract

As the number of detected rocky extrasolar planets increases, the question of whether their surfaces could be habitable is becoming more pertinent. On Earth, the long-term carbonate-silicate cycle is able to regulate surface temperatures over timescales larger than one million years. Elevated temperatures enhance weathering, removing CO_2 from the atmosphere, which is subducted into the mantle. At mid-ocean ridges, CO_2 is supplied to the atmosphere from the interior. The carbon degassing flux is controlled by the melting depth beneath mid-ocean ridges and the spreading rate, influenced by the pressure- and temperature-dependent mantle viscosity. The influences of temperature and pressure on mantle degassing become increasingly important for more massive planets. Here, we couple a thermal evolution model of Earth-like planets of different masses with a model of the long-term carbon cycle and assess their surface temperature evolution. We find that the spreading rate at 4.5 Gyr increases with planetary mass up to 3 Earth masses, since the temperature dependence of viscosity dominates over its pressure dependency. For higher-mass planets, pressure dependence dominates and the plates slow down. In addition, the effective melting depth at 4.5 Gyr as a function of planetary mass has its maximum at $3\ M_\oplus$. Altogether, at 4.5 Gyr, the degassing rate and therefore surface temperature have their maximum at $3\ M_\oplus$. This work emphasizes that both age and mass should be considered when predicting the habitability of exoplanets. Despite these effects, the long-term carbon cycle remains an effective mechanism that regulates the surface temperature of massive Earth-like planets.

1. Introduction

Exoplanets are being discovered at a rapid rate. NASA's Kepler space telescope identified more than 4000 new planet candidates (Fulton et al. 2017), and advances in detection techniques are yielding observations of a vast array of distinct worlds (Madhusudhan et al. 2016). A significant fraction of currently known exoplanets have radii in between those of Earth and Neptune, $R_P = 1.0$–$3.9\ R_\oplus$ (Batalha et al. 2013). The density of planets in this group with a radius smaller than $1.6\ R_\oplus$ is generally consistent with a rocky composition, as opposed to the larger planets having lower densities, seemingly suggesting a low-density envelope (Fulton et al. 2017; Lozovsky et al. 2018). Although these small planets are strikingly common around Sun-like stars (Marcy et al. 2014), they have also been identified orbiting low-mass stars. In the near future, the only properties of exoplanets that will be able to be explored beyond their ages, masses, and radii are their atmospheres. For a few planets detailed information on their atmospheric compositions has been gathered, and this will be extended to more super-Earths in the habitable zone in the near future by spectroscopic studies done by the Extremely Large Telescope and the James Webb Space Telescope (Dorn et al. 2018).

The prospect of finding conditions at which liquid water is stable on a planetary surface is exciting. Conditions that allow for liquid water would need to be present for extended periods

of time for life to develop and to be sustained. A critical factor in the regulation of the surface climate is the long-term carbon cycle (Franck et al. 2000; Kadoya & Tajika 2014, 2015; Haqq-Misra et al. 2016; Mills et al. 2019; Isson et al. 2020).

Volcanic systems have vented CO_2 from Earth's mantle into the atmosphere for billions of years (Kasting & Catling 2003). Since silicate weathering and thereby the removal rate of CO_2 from the atmosphere depend on atmospheric CO_2 and surface temperature, a negative feedback is established. While these reactions have first been described by Urey (1952), the importance of the long-term carbon cycle as a feedback mechanism regulating the climate evolution of Earth and other planets has been described later (Walker et al. 1981; Kasting 1989).

Carbon reaches the atmosphere from the deeper parts of Earth through volcanism. At mid-ocean ridges, lithospheric plates diverge and mantle rock ascends to replace it. In the process, decompression melting takes place and carbon is degassed. The rate of carbon degassing is of fundamental importance, as it influences the width of the habitable zone both for stagnant-lid (Noack et al. 2017) and plate tectonics planets (Kadoya & Tajika 2014). At the outer boundary, inefficient carbon degassing could lower the surface temperature to below the freezing point of water, while at the inner boundary high degassing rates could enhance surface temperatures and cause water evaporation (Noack et al. 2017).

Degassing rates depend on the convective regime. While in the solar system Earth is the only planet with active plate tectonics, the dominating tectonic regime on super-Earths is a matter of debate (Kite et al. 2009). Noack et al. (2017) and Dorn et al. (2018) explore degassing rates for super-Earths in a stagnant-lid regime and find that degassing is most efficient on 2–3 $M_\oplus$ planets ($M_\oplus$ is the mass of Earth), depending on the

---

initial mantle temperature of these planets. In this study, we explore the degassing flux and surface temperature for super-Earths with a mass between $M_\oplus = 1$ and 10 with active plate tectonics. To this end, we couple a parameterized model of mantle convection to a model of the long-term carbon cycle. In contrast to previous carbon cycle models, we model the degassing flux by including temperature- and pressure-dependent mantle viscosity and by explicitly calculating the melting depth beneath mid-ocean ridges.

2. Model Setup

Our model connects the long-term carbon cycle to the thermal evolution of plate tectonics planets of different masses. Carbon is degassed from the mantle reservoir R_{man} into the atmospheric reservoir R_{atm} by the degassing flux F_{deg}. Exposed weatherable rock reacts with atmospheric CO_2 to form bicarbonate and calcium and magnesium ions, which are washed into the oceans, where they convert to carbonate minerals. An increase of CO_2 in the atmosphere speeds up silicate weathering, composed of the continental weathering flux F_w and the seafloor weathering flux F_{sfw}, both of which draw CO_2 from the atmosphere. Carbon is added to the plate reservoir R_p and subsequently transported by the subduction flux F_{sub}. A fraction of the subducted carbon is directly degassed back into the atmosphere at arc volcanoes (F_{arc}), while the rest enters the mantle, completing the long-term carbon cycle.

The basic carbon cycle model outlined above has been discussed extensively in the literature (Walker et al. 1981; Sleep & Zahnle 2001; Kasting & Catling 2003; Foley 2015), and the main equations are given in Appendix A. Here, we focus on the degassing rate and its evolution through time for different planetary masses. Degassing at mid-ocean ridges is the dominant pathway for carbon to reach the surface from the mantle (Orcutt et al. 2019) and is therefore crucial for the long-term carbon cycle. In previous studies, the degassing flux has often been taken as a predefined input flux when considering Earth's evolution (Krissansen-Totton & Catling 2017; Kadoya et al. 2020) or taken to be controlled by the mantle carbon reservoir when considering the evolution of Earth-sized planets (Sleep & Zahnle 2001; Höning et al. 2019). Foley (2015) introduced a dependence of the plate velocity—and thereby degassing rate—on the surface temperature but found that the effect on the degassing rate for planets in the habitable zone is small. Oosterloo et al. (2021) calculated the plate velocity as a function of the mantle heat flow but kept the melting depth constant and did not account for the pressure dependence of mantle viscosity, making an application to more massive planets challenging. Kadoya & Tajika (2015) also neglected the pressure dependence of viscosity when considering the carbon cycle for exoplanets.

Following Sleep & Zahnle (2001) and Foley (2015), the degassing flux F_{deg} is given by

$$F_{deg} = f_d \frac{R_{man}}{V_m} 2 v_p L d_{melt}, \qquad (1)$$

where f_d is the fraction of upwelling mantle that degasses, v_p the plate velocity, L the length of ridges, and d_{melt} the depth where melting begins. Values for the parameters used in this study can be found in Table 1. The carbon density of a planet is given by the ratio between the mantle carbon reservoir R_{man} and the

Table 1
Parameters Used in This Study

Parameter		Value	References
$M_\oplus$	Mass of Earth	5.9736×10^{24} kg	(1)
f_d	Fraction mantle that degasses	0.32	(2)
κ	Mantle thermal diffusivity	10^{-6} m^2 s^{-1}	(3)
Ra_{crit}	Critical Rayleigh number	1100	(3)
α	Thermal expansivity	2×10^{-5} K^{-1}	(3)
β	Scaling exponent	1/3	(3)
η_0	Viscosity	10^{21} Pa s	(3)
E_a	Activation energy	335 kJ mol^{-1}	(3)
$E_{a,lm}$	Activation energy lower mantle	300 kJ mol^{-1}	(3)
V_a	Activation volume	4 cm^3 mol^{-1}	(3)
$V_{a,lm}$	Activation volume lower mantle	2.5 cm^3 mol^{-1}	(3)
C_{tot}	Bulk silicate Earth carbon budget	5.56×10^{20} kg	(5)
C_p	Mantle heat capacity	1200 J kg^{-1} K^{-1}	(3)
$C_{p,c}$	Core heat capacity	840 J kg^{-1} K^{-1}	(3)
R_{gas}	Ideal gas constant	8.314 J mol^{-1} K^{-1}	(3)
P_{ref}	Reference pressure	0	(3)
T_{ref}	Reference temperature	1600 K	(3)
$T_{p,i}$	Initial mantle potential temperature	2520 K	(3)
k	Mantle thermal conductivity	4.2 W m^{-1} K^{-1}	(3)
A_1	Constant	1 397.273 K	(4)
A_2	Constant	137.863 K	(4)
A_3	Constant	-5.722	(4)

References. (1) Turcotte & Schubert 2002; (2) Foley 2015; (3) Schaefer & Sasselov 2015; (4) Hirschmann 2000; (5) Hirschmann 2018.

mantle volume V_m. In the following, we will focus on the parameters v_p and d_{melt}, which differ substantially as a function of planet mass and thereby control the surface habitability.

With increasing planetary mass, the pressure increases, leading to an increase of the mantle viscosity. According to Tackley et al. (2013), the core–mantle boundary (CMB) region on a 10 $M_\oplus$ planet with an Earth-like composition experiences a 10 times pressure increase. This significant pressure increase substantially slows down mantle convection (Miyagoshi et al. 2013). Van den Berg et al. (2019) show that the effect of increasing mass on viscosity could result in a viscosity of two orders of magnitude higher for an 8 $M_\oplus$ planet than for an Earth-sized planet. This increase in viscosity for higher-mass planets is further supported by Schaefer & Sasselov (2015), who show that an $M = 5$ planet develops a mantle viscosity up to two orders of magnitude higher when a pressure-dependent viscosity case is considered as opposed to a pressure-independent viscosity, underscoring the importance of including the pressure effect on viscosity. However, higher-mass planets do not solely imply an increase in internal pressures, but also exhibit higher internal temperatures. For example, retention of primordial heat could be higher owing to a relatively smaller ratio of surface area to planetary volume or to ineffective convective heat transport caused by the higher pressure affecting viscosity.

We base our interior thermal evolution model on Schaefer & Sasselov (2015) and derive the plate velocity in Equation (1)

from boundary layer theory (Schubert et al. 2001),

$$v_p = \frac{5.38\kappa(R_p - R_c)}{\delta_u^2}, \tag{2}$$

where κ is the mantle thermal diffusivity, R_p and R_c are the radius of the planet and core, respectively, and δ_u is the upper boundary layer thickness, given by

$$\delta_u = D\left(\frac{\mathrm{Ra_{crit}}}{\mathrm{Ra}}\right)^\beta = \left(\frac{\kappa\eta(\langle T_m\rangle, P_{\mathrm{mm}})\mathrm{Ra_{crit}}}{g\alpha\rho_m\Delta T}\right)^\beta, \tag{3}$$

where D is the mantle thickness, $\eta(\langle T_m\rangle, P_{\mathrm{mm}})$ is the effective mantle viscosity with the mid-mantle pressure P_{mm} and the spherically averaged mantle temperature $\langle T_m\rangle$, α is the thermal expansivity, ΔT is the superadiabatic temperature increase throughout the mantle, and Ra and $\mathrm{Ra_{crit}}$ are the Rayleigh and critical Rayleigh number, respectively.

Since, in contrast to Schaefer & Sasselov (2015), we do not model the deep water cycle, we calculate the viscosity for dry silicate material following Stamenković et al. (2011, 2012). The effective viscosity is then given by

$$\eta(\langle T_m\rangle, P_{\mathrm{mm}}) = \eta_0 \exp\left\{\frac{E_a}{R_{\mathrm{gas}}}\left(\frac{1}{\langle T_m\rangle} - \frac{1}{T_{\mathrm{ref}}}\right)\right. \\ \left. + \frac{1}{R_{\mathrm{gas}}}\left(\frac{P_{\mathrm{mm}}V_a}{\langle T_m\rangle} - \frac{P_{\mathrm{ref}}V_{a,\mathrm{ref}}}{T_{\mathrm{ref}}}\right)\right\}, \tag{4}$$

where the values for the reference temperature and pressure are taken to be 1600 K and 0 Pa, respectively, and the pressure-dependent activation volume is given by the scaling law derived by Stamenković et al. (2011),

$$V_a = \left(1.38 + 2.15\right. \\ \left. \cdot \exp\left[-0.065\left(\frac{P_{\mathrm{mm}}}{10^9} + 10\right)^{0.485}\right]\right) \cdot 10^{-6}. \tag{5}$$

The average temperature follows from an adiabatic temperature profile extrapolated to the surface (Schaefer & Sasselov 2015),

$$\langle T_m\rangle = \frac{3}{R_p^3 - R_c^3}\int_{R_c}^{R_p} r^2 T_{\mathrm{ad}}(r)dr, \tag{6}$$

with the adiabatic temperature profile

$$T_{\mathrm{ad}}(r) = T_p + T_p\frac{\alpha g}{c_p}\Delta r, \tag{7}$$

where T_p is the potential temperature of the mantle.

We calculate the thickness of the lower thermal boundary layer similar to the upper thermal boundary layer (Equation (3)) but use a local instability criterion, since the high pressure at the CMB substantially influences the heat flow here. This calculation differs from the calculation of the upper boundary layer thickness (Equation (3)), which depends on the convection rate of the whole mantle and therefore requires the use of an effective viscosity.

The thickness of the lower thermal boundary layer δ_l can then be calculated as

$$\delta_l = \left(\frac{\kappa\eta(T_c, P_c)\mathrm{Ra_{crit}}}{g\alpha\rho_m(T_c - T_l)}\right)^\beta, \tag{8}$$

where T_c and P_c are the temperature and pressure at the CMB, respectively, and T_l is the temperature at the top of the lower thermal boundary layer.

The initial core temperature $T_{c,i}$ is estimated using a scaling law derived by Stixrude (2014),

$$T_{c,i} = T_{c,i\oplus}\left(\frac{P_c}{140}\right)^{0.48}, \tag{9}$$

where $T_{c,i\oplus} = 4180$ K (Fiquet et al. 2010). Following Schaefer & Sasselov (2015), we assume an initial mantle potential temperature of 2520 K for all planetary masses in our reference model, which translates into an initial average mantle temperature of 3000 K for Earth, increasing with planetary mass. The effect of assuming different initial mantle potential temperatures is assessed separately (Section 3.3). Calculating the heat fluxes out of the core and mantle, we apply a standard parameterized thermal evolution model from Schubert et al. (2001), which is described in Appendix B.

In addition to the plate velocity, the mantle melting depth must be calculated in order to determine the degassing flux. Since we consider melting at mid-ocean ridges, we follow Kite et al. (2009) and assume that melting occurs as long as the mantle potential temperature is higher than the zero-pressure solidus. The melting depth is considered to be the region between the surface and the point where the solidus crosses the adiabatic temperature gradient ($T_{\mathrm{sol}} > T_{\mathrm{grad}}$), as seen in Figure 1. Since with increasing planetary mass planets are expected to cool more slowly or even heat up, the melting depth increases with time relative to 1 $M_\oplus$ planets (Papuc & Davies 2008).

The solidus curve for pressures up to 10 GPa is given by Hirschmann (2000),

$$T_{\mathrm{sol}} = 1397.273 + 137.863P - 5.722P^2, \tag{10}$$

and for pressures between 10 and 12 GPa, the solidus temperature is given by a later work from the same authors (Hirschmann et al. 2009),

$$T_{\mathrm{sol}} = -1.092(P - 10)^2 + 32.39(P - 10) + 2208.15. \tag{11}$$

For pressures higher than 12 GPa, the solidus temperature becomes irrelevant, since any produced melt is likely unable to rise to the surface: the P-T location of crystal-liquid density inversions is determined by the compressibility, phase equilibria, and element partitioning (Agee 1998). At high pressures, density inversions are most likely if the liquid has a high compressibility relative to the crystalline phase, when the crystalline phase is stable over a large pressure range or when the liquid is "chemically dense" (Agee 1998). According to Agee (1998), crystal-liquid density inversions occur in Earth in the transition zone and lower mantle, due to the extensive stability range of phases such as garnet and perovskite. For simplicity, we follow Noack et al. (2017) and use a fixed value of 12 GPa as estimated by Agee (1998) and Ohtani et al. (1995). In our model, we impose a limit to the effective melting depth at this pressure.

As noted above, the remaining carbon fluxes are calculated following standard carbon cycle models (Sleep & Zahnle 2001; Foley 2015) and given in Appendix A. All parameters that directly depend on the size and/or mass of the planet (such as subduction zone length, land area, and gravity) are adjusted accordingly. For Earth-sized planets, the initial carbon distribution
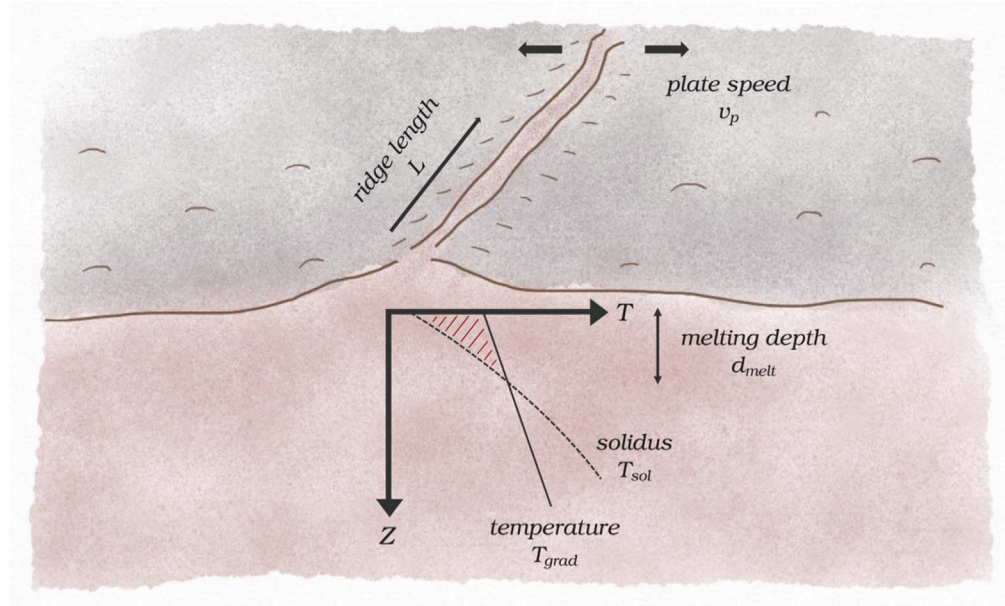
Figure 1. The melting region at mid-ocean ridges is determined by the depth at which melting begins d_{melt}. The production rate of oceanic crust additionally depends on the plate speed v_p and the ridge length L.

between the atmosphere, crust, and mantle has been shown to become unimportant after 1 Gyr (Foley 2015; Höning et al. 2019). For simplicity, we assume for our reference model that all carbon is initially stored in the mantle, but we will elaborate on the effect of the initial carbon distribution in Section 3.3. We also do not explicitly model ocean chemistry, which only affects the climate on considerably shorter timescales, since the carbonate-silicate cycle takes over control of the system on timescales longer than ≈ 1 Myr (Sundquist 1991; Colbourn et al. 2015; Höning 2020).

Valencia et al. (2006, 2007) calculate the interior structure of super-Earths up to 10 $M_\oplus$. The authors find that the dependence of several parameters on mass can be adequately described by a power-law relationship of the form

$$Z = Z_\oplus \left(\frac{M}{M_\oplus} \right)^\xi, \tag{12}$$

where Z is the considered parameter and ξ is a scaling exponent. In this way parameters such as gravitational acceleration, mantle density, and planetary radius can be related to planet mass. For example, we use the following power law for the mantle density ρ_m:

$$\rho_m = \rho_{m\oplus} \left(\frac{M}{M_\oplus} \right)^{0.195}. \tag{13}$$

Values for ξ for the other scaled parameters can be found in Table 2.

3. Results

We first focus on the effective melting depth at 4.5 Gyr for planets with masses between 1 and 10 $M_\oplus$ (Section 3.1). In Section 3.2, we elaborate on the interior and surface temperature evolution, and Section 3.3 addresses the effects of different initial mantle temperatures and carbon concentrations.

Table 2
Parameters That Are Scaled According to Mass, from Valencia et al. (2006)

Parameter	Description	Baseline Value	ξ
R	Planetary radius	6371 km	0.269
R_c	Core radius	3480 km	0.247
g	Gravitational acceleration	9.81 km	0.462
ρ_m	Mantle density	3300 kg m^{-3}	0.195
R_{man}	Bulk silicate Earth carbon budget	5.56×10^{20} kg	1
L	Subduction zone length	6×10^7 m	0.269

3.1. Effective Melting Depth and Plate Thickness at 4.5 Gyr

The melting depth is a main parameter controlling the surface temperature in our model, as it directly affects the degassing rate. With increasing planetary mass, both the mantle temperature at 4.5 Gyr and the solidus temperature increase, which are competing factors determining the melting depth. In addition, the 12 GPa limit to positively buoyant melt moves to shallower depth. This limit is imposed to account for the densification of magmatic liquids up to the point where the melt will become neutrally or even negatively buoyant with respect to coexisting minerals (Ohtani et al. 1995; Agee 1998). All three parameters for different planetary masses are illustrated in Figure 2, where the effective melting depth is marked. It becomes apparent that as long as the melting depth is reached for pressures below the 12 GPa limit, the melting depth at 4.5 Gyr steadily increases with planetary mass. In contrast, for planets whose effective melting depth is determined by the 12 GPa limit, this depth decreases with increasing planetary mass. Therefore, a peak in the melting depth for intermediate planetary masses is expected.

In Figure 3, we show (a) the effective melting depth and (b) the plate thickness at 4.5 Gyr as a function of planetary mass. For the effective melting depth, we find a minimum at 3 $M_\oplus$. On the one hand, the mantle temperature generally increases more strongly with planetary mass than the solidus temperature does, resulting in an increase of the melting depth. On the other hand, the 12 GPa limit moves to shallower depths, which
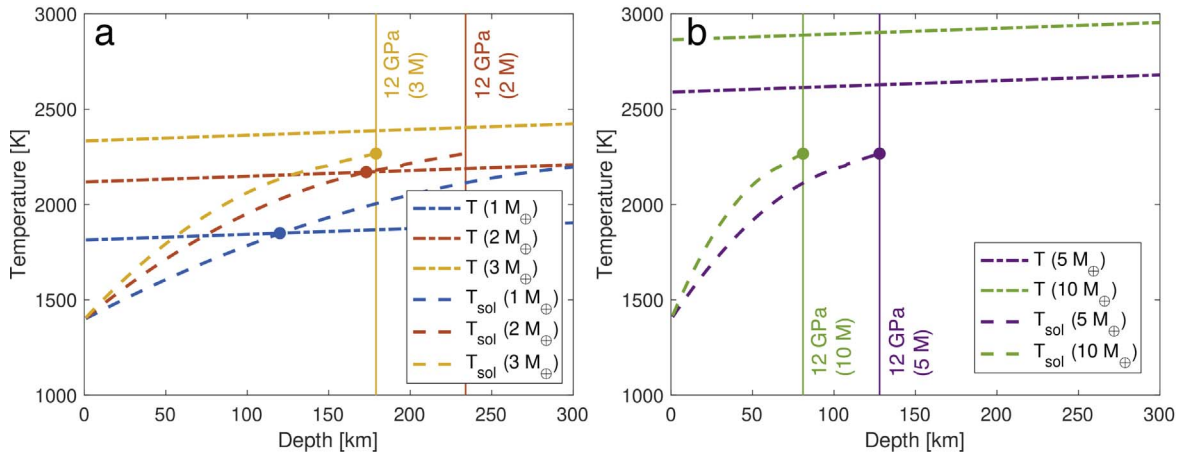
Figure 2. Temperature profile adiabatically extrapolated to the surface after 4.5 Gyr of the evolution (dashed–dotted) and solidus temperatures (dashed) for different planet masses. The thin solid lines correspond to the depth below which melt is negatively buoyant. The filled circles correspond to the effective melting depth, which is either the intersection between the temperature profile and the solidus temperature or the depths below which melt is negatively buoyant.
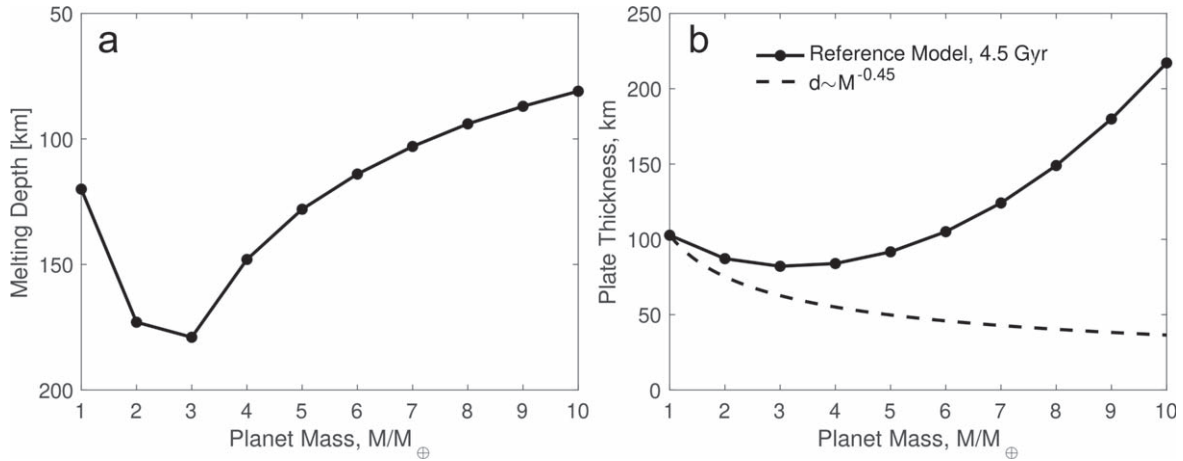

Figure 3. (a) Melting depth and (b) plate thickness at 4.5 Gyr as a function of planetary mass (dashed line: scaling extrapolation neglecting pressure-dependent viscosity after Valencia et al. 2007).

becomes dominant for planets from 3 $M_\oplus$. As a result, the effective melting depth, i.e., the depth that controls degassing, has its peak at 3 $M_\oplus$ (see Figure 3(a)).

For the plate thickness (Figure 3(b)), we also find a minimum at 3 $M_\oplus$. This is a result of the pressure dependence of viscosity, which dominates over its temperature dependence for planets more massive than 3 $M_\oplus$. Since the plate velocity directly follows from the boundary layer thickness (see Equation (2)), this effect also promotes high degassing rates particularly for planets of 3 $M_\oplus$. We note that this minimum does not exist for a model that neglects the pressure dependence of viscosity (dashed curve, following Valencia et al. 2007). Altogether, accounting for pressure-dependent viscosity, both the plate thickness and the melting depth promote a peak of the degassing rate at 4.5 Gyr for planets of ≈3 $M_\oplus$.

3.2. Climate Evolution for Different Planetary Masses

Increasing planetary mass generally implies a delayed cooling of the mantle or even an increasing temperature with time due to the higher mantle viscosity. As a consequence, more massive planets remain hotter for a longer period of time (Figure 4(a)). However, the plate velocity (Figure 4(c)) depends on the mantle viscosity and therefore not only on temperature but also on

pressure. From ≈1 to 4.5 Gyr, this combination results in a particularly high plate velocity for planets with 3 $M_\oplus$. This result, however, depends on the initial mantle temperature (discussed later, in Section 3.3). Since the degassing rate (Figure 4(d)) depends on both the plate velocity and the melting depth, its evolution is similar to that of the plate velocity, with an even stronger decrease of the degassing rate with time for 1 $M_\oplus$ planets compared to more massive planets. This is a consequence of the more rapid cooling of 1 $M_\oplus$ planets, which strongly reduces the melting depth with time.

The evolution of the surface temperature for different planetary masses is depicted in Figure 5 for models with (panels (a) and (c)) and without (panels (b) and (d)) solar evolution. For the models without solar evolution (panels (b) and (d)), we use the present-day solar luminosity, and for the models that consider solar evolution (panels (a) and (c)), the luminosity is assumed to increase linearly by 1/3 during 4.5 Gyr up to the present-day value (Ribas 2009). Other orbital and stellar parameters are kept at Earth's values. While panels (a) and (b) depict modeling results for an Earth-like planet with an emerged land fraction of 30%, panels (c) and (d) depict planets where the land fraction is reduced to 1%. For comparison with previous carbon cycle studies for 1 $M_\oplus$ planets, modeling results from
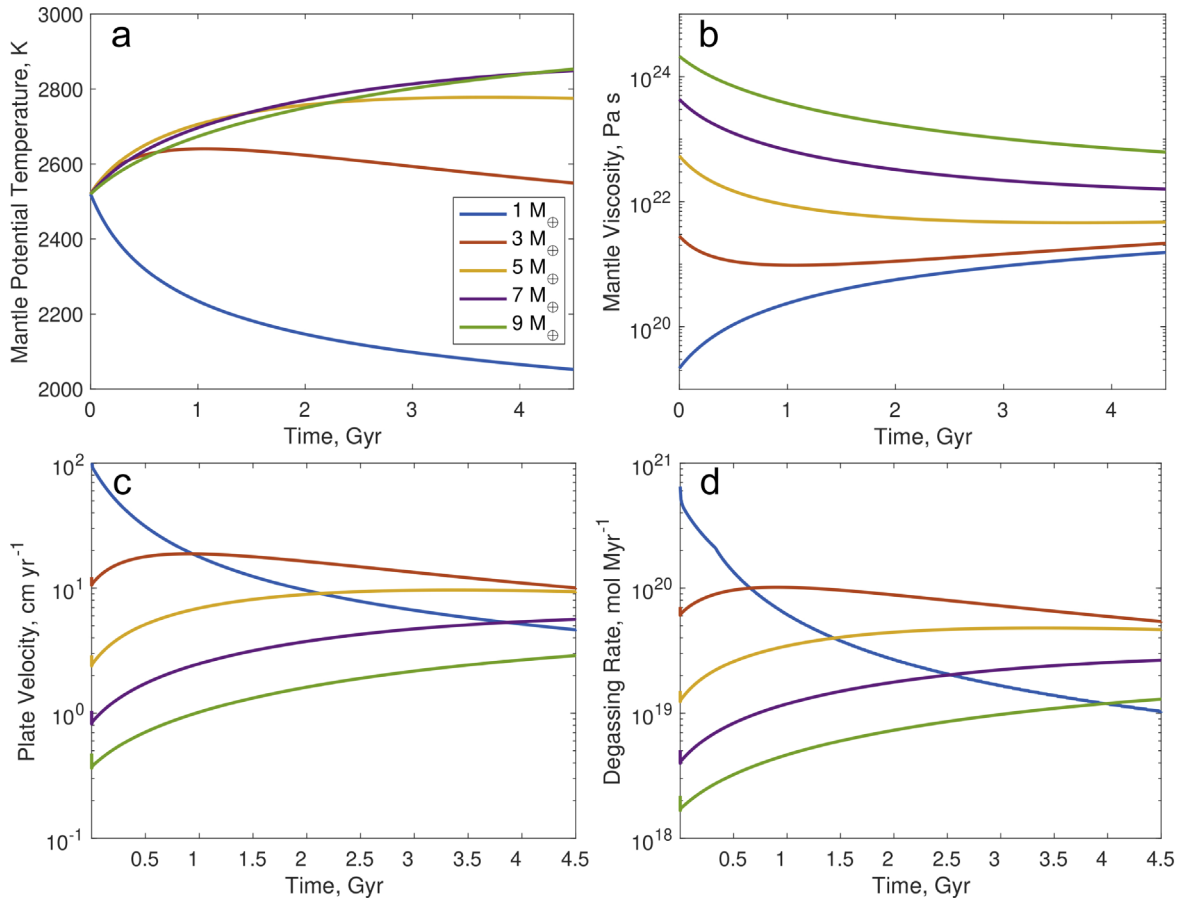
Figure 4. Evolution of (a) mantle potential temperature, (b) mantle viscosity, (c) plate velocity, and (d) degassing rate for different planet masses.

Foley ([2015](#)) are added to panel (a) and modeling results from Höning et al. ([2019](#)) are added to panels (c) and (d).

Since Foley ([2015](#)) neglected the effect of the interior evolution on the degassing rate, the temperature evolution in their model stays constant after an initial adjustment time (dashed curve in Figure [5](#)(a)). In contrast, our results indicate a steadily decreasing surface temperature for 1 $M_\oplus$ planets (solid blue in panel (a)) if solar evolution is neglected, since both the plate velocity and the melting depth decrease with time. The fact that both curves do not cross at 4.5 Gyr is because we do not scale the present-day degassing rate to match a predefined value. For intermediate planet masses (red and yellow curves in panel (a)), the surface temperature does not substantially vary over time, and for high-mass planets (purple and yellow curves), the surface temperature steadily increases. If solar evolution is considered, the low- and intermediate-mass planets in Figure [5](#)(b) have the smallest temperature variation throughout the past 3 Gyr, as the mantle temperature decreases with time (or, at least, does not significantly increase). We also find that the most massive planets have a surface temperature below the freezing point of water in their early evolution (discussed in more detail in Section [4](#)).

Considering a planet with only 1% emerged land area (Figures [5](#)(c) and (d)), the differences between planets of different masses increase, since climate regulation does not work as efficiently in the absence of a substantial contribution of temperature-dependent continental weathering. However, the trend found in Figures [5](#)(a) and (b) for the surface temperature evolution for different planetary masses remains the same. For

comparison, the dotted curve shows modeling results from Höning et al. ([2019](#)), considering a carbon cycle with a temperature-dependent arc-volcanism flux for water-covered planets of 1 $M_\oplus$. While both modeling results suggest a decreasing surface temperature if solar evolution is neglected, the surface temperature in our model with a degassing rate dependent on plate velocity and melting depth depends on the thermal evolution more strongly. We also find that the high initial degassing rate for 1 $M_\oplus$ planets, in combination with the limited weathering rate due to the small land fraction, implies hot, potentially uninhabitable surface conditions during the first 0.5 Gyr.

3.3. Initial Mantle Temperature and Carbon Budget

For Earth-sized planets the temperature dependence of viscosity ensures that the late evolution hardly depends on the initial mantle temperature (Schubert et al. [2001](#)). This does not necessarily apply to more massive planets if the pressure dependence of viscosity is considered (Schaefer & Sasselov [2015](#)). For massive planets, the degassing rate at 4.5 Gyr and therefore the atmospheric CO_2 abundance increase with the initial mantle temperature, resulting in higher surface temperatures (see Figure [6](#)(a)). However, the planet mass that yields the highest surface temperature at 4.5 Gyr is not very sensitive to the initial mantle temperature: in most cases, the peak remains at 3 $M_\oplus$, even though the initial mantle temperature is varied over a large range. However, for very high initial mantle temperatures, the peak is slightly shifted toward higher planet masses: for
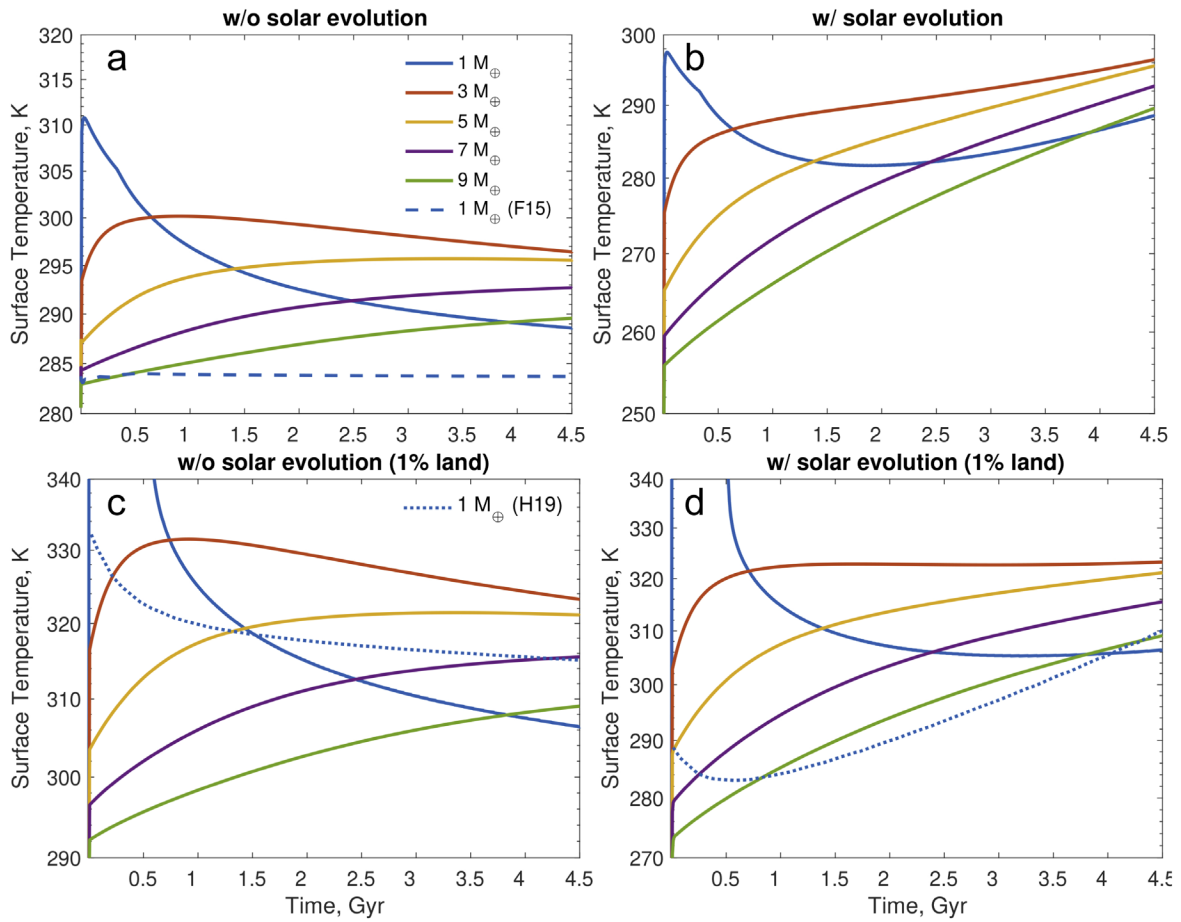
Figure 5. Surface temperature evolution without (left) and with (right) solar evolution for our reference model of 30% land area (top) and a reduced land area of 1% (bottom). The dashed line in panel (a) corresponds to the results of Foley (2015), and the dotted lines in panels (c) and (d) correspond to the results of Höning et al. (2019).

example, for a very high initial potential temperature of 2750 K, we find the peak at 4 $M_\oplus$ (Figure 6(a)).

Interestingly, numerical models of stagnant-lid planets (Dorn et al. 2018) show a similar behavior, even though in these models the degassed CO_2 accumulates in the atmosphere over the entire evolution of the planet and is not only determined by the degassing rate at 4.5 Gyr. While Dorn et al. (2018) find a maximum degassed CO_2 for 3 $M_\oplus$ for an initial mantle temperature of 2000 K, this peak is shifted toward 2 $M_\oplus$ for an initially very low mantle temperature of 1600 K. Similarly, Noack et al. (2017) find a peak in surface temperature at 4.5 Gyr for planets between 2 and 4 $M_\oplus$ with a shift of the peak with higher initial mantle temperatures toward higher planet masses. We note that the effect of the initial mantle temperature on the surface temperature at 4.5 Gyr is stronger for stagnant-lid than for plate tectonics planets, since the initial mantle temperature particularly controls early degassing, which makes up a significant part of the accumulated degassed CO_2 abundance on stagnant-lid planets in their late evolution.

The chemical composition of rocky exoplanets is thought to vary greatly (Bond et al. 2010; Moriarty et al. 2014; Madhusudhan et al. 2016). Even for Earth it is still debated which combination of meteorites best represents Earth's bulk chemical composition (Moynier & Fegley 2015). In order to assess the effect of the planetary carbon density on the habitability of super-Earths, we ran models varying the carbon concentration and present the results in Figure 6(b), keeping the

land fraction constant at present-day Earth's value. Since the atmospheric CO_2 is controlled by the degassing rate, which in turn depends linearly on the mantle carbon concentration, our results do not change qualitatively. Similar to Figure 6(a), we find a maximum surface temperature at 4.5 Gyr for planets of 3 $M_\oplus$. The effect of planetary mass becomes more pertinent for higher bulk carbon concentrations, which has important implications for assessing the habitability of exoplanets: Kopparapu et al. (2013) argue that around 340 K the moist-greenhouse effect is reached, where the stratosphere becomes water dominated and hydrogen loss to space occurs. This state can be considered as the inner edge of the habitable zone. For carbon-rich planets near the inner edge of the habitable zone, it is therefore crucial to consider the planetary mass when assessing the potential for life.

Figure 6(c) shows the effect of the initial carbon distribution between the mantle and the atmosphere on the evolution of the surface temperature (solid: all carbon initially in the mantle; dashed: all carbon initially in the atmosphere). While for planets of 1 $M_\oplus$ (blue) the initial carbon distribution is negligible, more massive planets need a longer period of time to redistribute their carbon: a planet of 5 $M_\oplus$ eliminates the effect of the initial distribution after 1.5 Gyr, and a planet of 9 $M_\oplus$ is still slightly affected by the initial carbon distribution at 4.5 Gyr. This trend is supported by Figure 6(d), which shows the surface temperature at 4.5 Gyr as a function of planet mass with all carbon initially in the mantle (solid), in the atmosphere
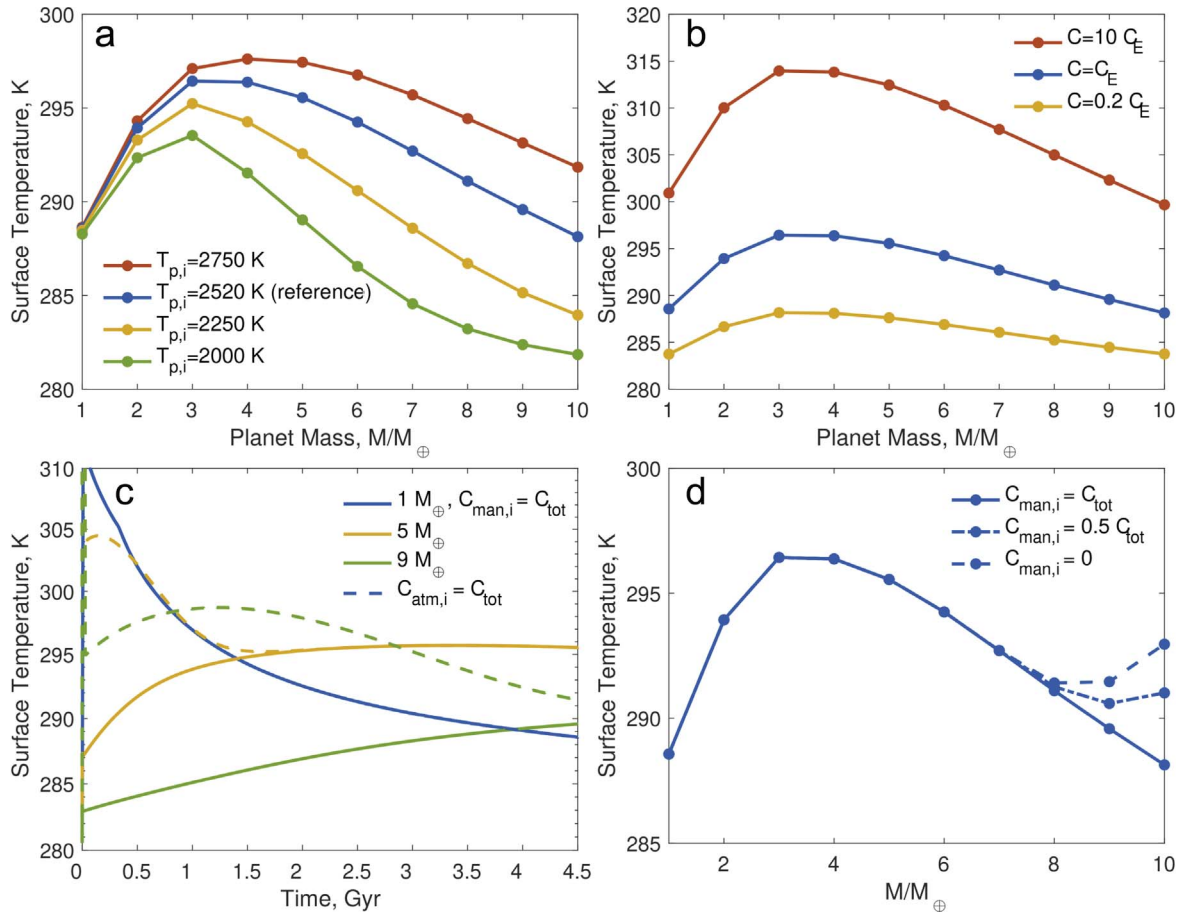
Figure 6. Top panels: surface temperature at 4.5 Gyr as a function of planet mass for different (a) initial mantle temperatures and (b) bulk carbon densities C relative to Earth's bulk carbon density C_E. Panel (c) compares the surface temperature evolution between planets with all carbon initially in the mantle (solid) and planets with all carbon initially in the atmosphere (dashed), and panel (d) depicts the surface temperature at 4.5 Gyr as a function of planet mass for different initial carbon distributions between the two reservoirs.

(dashed), and equally distributed between the two reservoirs (dashed–dotted).

4. Discussion

Coupling a model of the long-term carbon cycle to thermal evolution models with temperature- and pressure-dependent viscosity and to a model of the melting depth, we assessed the influence of planetary mass on the surface temperature evolution of Earth-like planets. In this section, we compare our model to previous studies and discuss simplifications and limitations of our model, as well as consequences for the habitability of exoplanets.

Starting with Walker et al. (1981), models of the long-term carbon cycle for Earth and other planets have been used to assess the climate evolution on Earth and other plate tectonics planets (Sleep & Zahnle 2001; Kasting & Catling 2003; Foley 2015). A key parameter that influences the climate on long timescales is the mantle degassing rate, which is balanced by the weathering rate for specific values of atmospheric CO_2 and surface temperature. For Earth's evolution, it is suitable to approximate the degassing rate over time with scaling laws (Krissansen-Totton & Catling 2017; Krissansen-Totton et al. 2018; Kadoya et al. 2020), but in particular an extrapolation of the model to planets of different masses requires the consideration of the interior evolution.

Rushby et al. (2018) modeled the carbon cycle for planets of different masses by setting the degassing rate proportional to the internal heat production rate, thereby neglecting effects of the planet mass on the mantle viscosity and melting depth. As a result, they find only a little influence of planet mass on surface temperature, with a small trend toward higher surface temperature with increasing mass (<3 K difference between 1 and 10 $M_\oplus$). However, this simplification neglects the fact that the melting depth below mid-ocean ridges crucially depends on the pressure–temperature profile and that the mantle heat flow (which controls the plate velocity) is determined by pressure- and temperature-dependent viscosity. In contrast, we find a peak in the surface temperature for 3 $M_\oplus$ planets, which is ≈ 8 K above the surface temperature for a 1 $M_\oplus$ planet. At higher masses, the surface temperature at 4.5 Gyr decreases again and may even fall below the surface temperature that is found for a 1 $M_\oplus$ planet. Whereas planets of 1 $M_\oplus$ have their highest mantle temperature and therefore degassing rate throughout the first 1 Gyr, after which the initial mantle temperature becomes unimportant (Schubert et al. 2001), the mantle temperature of more massive planets is much longer influenced by its initial value. Regardless of that, at 4.5 Gyr we find a peak in the surface temperature that is hardly influenced by initial conditions.

Kadoya & Tajika (2015) include a thermal evolution model of the planetary interior and calculate the degassing rate as a

function of melting depth and plate velocity for planets up to $5\,M_{\oplus}$. These authors use a viscosity law that neglects a pressure dependence, which results (a) in a steadily increasing degassing rate with planetary mass and (b) in a steadily decreasing degassing rate with time for all planetary masses. These results are in accordance with Oosterloo et al. (2021), who calculate the plate velocity from a thermal evolution model of the mantle and derive the surface temperature evolution for different compositions and masses. In contrast, our results indicate that these trends do not hold if a pressure dependence of viscosity is considered. In addition, we find that including a pressure limit to the melting depth substantially reduces the melting depth for massive planets.

The peak in surface temperature at 4.5 Gyr for planets of $\approx 3\ M_{\oplus}$ is similar to what has been found for stagnant-lid planets using numerical models of mantle convection in combination with a parameterization of the degassing rate (Noack et al. 2017; Dorn et al. 2018). The reason for this is similar: First, the pressure dependence of viscosity inhibits efficient heat flow and thereby high convection rates (or plate velocities in our model) for massive planets, whereas $1\ M_{\oplus}$ planets have already cooled down more strongly at 4.5 Gyr. Second, the increasing mantle temperature with planetary mass generally increases the melting depth up to the imposed pressure limit to degassing, which reduces the effective melting depth for planets larger than $3\ M_{\oplus}$.

Whether or not plate tectonics operate on exoplanets is a matter of debate and may depend on the plate thickness (Valencia et al. 2007), plate buoyancy (Kite et al. 2009), and temperature (Foley et al. 2012; Noack & Breuer 2014). Even for Earth, a transition from a stagnant-lid tectonic regime to modern plate tectonics may have occurred ≈ 3 billion years ago (Næraa et al. 2012; Gerya 2014). We note, however, that the surface temperature at 4.5 Gyr is hardly influenced by the nature of the early tectonic regime, as the atmospheric CO_2 is controlled by an equilibrium between degassing and weathering, with a residence time of CO_2 in the atmosphere that is far shorter than the timescale of interest here. Nevertheless, the influence of planetary mass on the likelihood of plate tectonics is crucial, as it determines the applicability of our model. Plate tectonics is promoted by the localization of shear and the weakening of a lithosphere with a high viscosity. Weakening of the lithosphere can be caused by the formation of microcracks, defects, or the reduction of grain sizes (Bercovici & Ricard 2014). Damage theory specifies this weakening of material. The damage mechanism described in Foley et al. (2012) is a feedback system between grain-size reduction by deformation and a grain-size-dependent viscosity: deformation reduces grain sizes, lowering the viscosity, resulting in more deformation. Larger planets exhibit lower healing of the lithosphere and higher convective stresses, and subsequently both factors increase the likelihood of plate tectonics to occur. Higher surface temperatures would promote the healing of the lithosphere by grain growth. Therefore, Foley et al. (2012) conclude that plate tectonics is more likely to occur on larger planets, preferably with cooler surface temperatures. Modeling results by Noack & Breuer (2014) indicate a peak likelihood for plate tectonics for planet masses between $M = 1$ and $M = 5$, suggesting that the effect of pressure on viscosity has a large influence on the occurrence of plate tectonics. Altogether, plate tectonics on planets somewhat more massive than Earth seems to be likely, although further studies are certainly needed.

An additional simplification of our model is the assumption of a constant land area. However, Abbot et al. (2012) argue that lower land fractions should be expected for the more massive terrestrial planets. A planet's mass increases more strongly than its surface area, which results in deeper oceans. The higher gravity furthermore reduces topography and creates shallower ocean basins (Cowan & Abbot 2014), increasing the surface area covered with water.

Considering stellar evolution (Figure 5(b)), the temperatures found in the early evolution for massive planets are slightly below the freezing point of water. However, this does not necessarily imply a snowball state, since these temperatures should be regarded as globally averaged values and do not rule out an equatorial section with temperatures above freezing. According to Warren et al. (2002), at surface temperatures above 261 K ice layers are too thin (<1 m) to form coherent sheets. This point is supported by Feulner & Kienert (2014), who find that the lowest steady-state configuration for a partially ice-covered state in the Sturnian glaciation generates a global mean surface air temperature of 266 K. For the Marinoan glaciation the coldest temperature at which ice-free ocean regions still exist is 268 K. In fact, Ye et al. (2015) found preserved benthic macroalgae in the Marinoan-age Nantuo Formation in South China. According to the authors, this suggests that during glaciation muddy substrates existed in the photic zones, suggesting open-water areas in coastal environments. These areas might have acted as a shelter for benthic macroalgae. Together with photoautotrophs, macroalgae could have been part of coastal food webs and the carbon cycle, just as they are today in glacial environments. In addition, autotrophes that do not rely on solar energy could exist below an icy crust. Altogether, life as we know it on Earth could potentially still evolve under these conditions. Nevertheless, as discussed above, massive planets are expected to keep their internal heat longer than planets of $1\ M_{\oplus}$ (see Figure 4(a)). As a consequence, the degassing rate of massive planets remains high for a longer period of time, or even increases with time (see Figure 4(d)). In combination with increasing stellar luminosity, the surface temperature of a massive planet that is in the conservative habitable range in the early evolution would increase more strongly with time than that of a $1\ M_{\oplus}$ planet. We note that the initial mantle temperature affects the early degassing rate and could therefore also affect the onset time of habitability, but such a shift in time would not significantly affect the total duration of the habitable period. Altogether, with increasing mass of the planet, the time window for life to evolve on it appears to become smaller.

5. Conclusions

In this paper, we have coupled a model of the long-term carbon cycle to a thermal evolution model of the mantle with temperature- and pressure-dependent viscosity and applied it to different planet masses. In particular, we calculated the degassing rate dependent on the melting depth and plate velocity. Our conclusions are summarized below:

1. The planet mass plays an important role in the evolution of the degassing rate, which causes different points in time throughout their evolution where the atmospheric CO_2 reaches its maximum. While low-mass planets have a high atmospheric CO_2 content particularly in their early

evolution, high-mass planets are expected to build up CO_2-rich atmospheres later.

2. At 4.5 Gyr, surface temperature increases with planetary mass up to $\approx 3\ M_\oplus$, since (i) the temperature dependence of mantle viscosity dominates over its pressure dependence, which yields higher plate velocities with increasing planetary mass, and (ii) the melting depth increases with the mantle temperature. However, above $\approx 3\ M_\oplus$, the surface temperature decreases with planetary mass, since (i) the pressure dependence of viscosity dominates and (ii) a pressure limit above which melt is not positively buoyant reduces the effective melting depth.

3. Despite these effects of planetary mass, the long-term carbon cycle remains an important stabilizing feedback mechanism for massive Earth-like planets for a wide range of bulk carbon densities.

Appendix A
Carbon Cycle Model

Seafloor weathering (Appendix A.1), continental weathering (Appendix A.2), and carbonate subduction (Appendix A.3) follow from standard carbon cycle models (Sleep & Zahnle 2001; Foley 2015). The parameter values that are used for the carbon cycle model can be found in Table A1. Parameters that directly depend on the planet size, such as land area or subduction zone length, are scaled accordingly.

A.1. Seafloor Weathering Flux

Seafloor weathering adds carbon to the oceanic plates, resulting in the withdrawal of CO_2 from the combined atmosphere and ocean reservoir. The CO_2 dissolved in seawater hydrothermally alters ocean floor basalt. Exactly how and to what extent the seafloor weathering flux operates is not fully understood at present. Brady & Gíslason (1997) showed that the CO_2 uptake during hydrothermal alteration directly depends on the partial pressure of CO_2 in the atmosphere, P_{CO_2}. In addition, seafloor weathering demands the supply of fresh rock, which is created at mid-ocean ridges. The plate velocity therefore dictates the supply of weatherable material. These parameters are combined in the following equation as given by Foley (2015):

$$F_{sfw} = F_{sfw}^* \left(\frac{v_p}{v_\oplus} \right) \left(\frac{P_{CO_2}}{P_{CO_2}^*} \right)^\alpha, \quad (A1)$$

where $v_\oplus$ is the modern-day plate speed on Earth. The plate speed v_p is derived in Equation (2), and as ratio to $v_\oplus$ depicts the effect of spreading rate. This makes the seafloor weathering flux mass dependent, where increasing planetary size results in a higher F_{sfw}. $P_{CO_2}^*$ is the partial pressure for Earth's conditions and $\alpha = 0.25$. The present-day value for the seafloor weathering flux is 1.75×10^{12} mol yr^{-1} as determined by Mills et al. (2014). Other scalings of seafloor weathering exist: Krissansen-Totton & Catling (2017) argue for a direct temperature dependence of basalt dissolution and therefore of seafloor weathering. The effect of the applied scaling on our results is expected to be small, since continental weathering (Appendix A.2) is the

Table A1
Parameter Values Used for the Carbon Cycle Model, Adopted from Foley (2015)

Parameter	Definition	Value
f_l	Land fraction	0.3
E_r	Maximum erosion rate	0.01 m yr^{-1}
ρ_r	Density of regolith	2500 kg m^3
m_{cc}	Average molar mass of Mg, Ca, K, Na	0.032 kg m^3
k_{cc}	Fraction of Mg, Ca, K, Na in crust	0.08
$S(4.5\ \text{Gyr})$	Present-day solar irradiance	1373 W m^{-2}
A	Albedo	0.31
σ	Stefan–Boltzmann constant	5.67×10^{-8} W m^{-2}
mCO_2	Molar mass of CO_2	0.044 kg mol^{-1}
T^*	Present-day temperature	285 K
T_e^*	Present-day effective temperature	254 K
PCO_2^*	Present-day partial pressure CO_2	33 Pa
F_w^*	Present-day weathering flux	12×10^{12} mol yr^{-1}
P_{sat0}	Reference saturation vapor pressure	610 Pa
T_{sat0}	Reference temperature	273 K
E_a	Activation energy silicate weathering	42×10^3 J mol^{-1}
a	P_{sat} exponent for silicate weathering	0.3
α	P_{CO_2} exponent for seafloor weathering	0.25
β	P_{CO_2} exponent for silicate weathering	0.55
P_{sat}^*	Present-day value saturation vapor pressure	1691 Pa
f	Fraction of subducted carbon that degasses	0.5
F_{sfw}^*	Present-day seafloor weathering flux	1.75×10^{12} mol yr^{-1}

dominating flux controlling the climate and directly depends on both temperature and atmospheric CO_2.

A.2. Continental Weathering Flux

The continental weathering flux F_w is calculated following Foley (2015) as follows:

$$F_w = F_{ws} \left(1 - \exp \left[-\frac{f_l F_w^*}{f_l^* F_{ws}} \left(\frac{P_{CO_2}}{P_{CO_2}^*} \right)^\beta \right. \right.$$
$$\left. \left. \times \left(\frac{P_{sat}}{P_{sat^*}} \right)^a \exp \left(\frac{E_a}{R_g} \left(\frac{1}{T^*} - \frac{1}{T} \right) \right) \right] \right), \quad (A2)$$

with the asterisk indicating values at present, f_l denoting the land fraction, E_a denoting the activation energy, and R_g denoting the universal gas constant. The exponents a and β are constants. A breakdown of the remaining parameters is provided in the following.

A kinetically limited continental weathering regime is assumed in this model. A kinetically controlled regime, although ill constrained, is suggested for Earth (West et al. 2005), indicating that the supply of weatherable bedrock exceeds the physical erosion rates necessary for complete denudation. In this regime, the parameter F_{ws} calculates the supply limit to weathering and is retrieved by Foley (2015) as follows:

$$F_{ws} = A_P \frac{f_l E_r k_{cc}}{m_{cc}} \rho_r, \quad (A3)$$

where f_l is the fraction of land above sea level that is subject to surface weathering; A_P is the surface area of the planet; E_r is the

erosion rate by physical processes; k_{cc} is the fraction of the cations Mg, Ca, K, and Na in the continental crust; ρ_r is the regolith density; and m_{cc} is the molar mass of the aforementioned cations.

With the supply limit to continental weathering established, three physical parameters remain to be determined for the weathering flux: the partial pressure of atmospheric CO_2, the temperature evolution of the atmosphere over time, and the saturation vapor pressure.

The partial pressure of atmospheric CO_2 can be related to the amount of carbon present in the atmosphere, R_{atm}. The initial value for R_{atm} is assumed to be zero, and CO_2 is added to the atmosphere by the degassing flux. The partial pressure affects the weathering rate by increasing the reaction rate with increasing P_{CO_2} and can be calculated by (Foley 2015):

$$P_{CO_2} = R_{atm} \frac{mCO_2}{A_P} g_P, \quad (A4)$$

where mCO_2 is the molar mass of CO_2.

The surface temperature can be derived by using the effective temperature T_e. The effective temperature depends on the amount of solar irradiation and the albedo:

$$T_e = \left(\frac{S(1 - A)}{4\sigma} \right)^{1/4}, \quad (A5)$$

where S the solar irradiance, A the albedo of the planet, and σ the Stefan–Boltzmann constant. For the model that considers stellar evolution, S is assumed to increase linearly by a factor of 1/3 throughout 4.5 Gyr (Ribas 2009). The surface temperature follows from the effective temperature (Foley 2015):

$$T = T^* + 2(T_e - T_e^*) + 4.6 \left(\frac{P_{CO_2}}{P_{CO_2}^*} \right)^{0.346} - 4.6, \quad (A6)$$

where T^*, T_e^*, and $P_{CO_2}^*$ are the surface temperature, effective temperature, and CO_2 partial pressure of present-day Earth, respectively. Finally, the saturation vapor pressure P_{sat} represents the fluctuation in runoff with changing surface temperature and can be calculated as follows (Foley 2015):

$$P_{sat} = P_{sat0} \exp \left[-\frac{m_w L_w}{R_g} \left(\frac{1}{T} - \frac{1}{T_{sat0}} \right) \right], \quad (A7)$$

with m_w denoting the molar mass of water, L_w the latent heat of water, P_{sat0} the reference saturation vapor pressure, and T_{sat0} the reference saturation vapor temperature.

A.3. Subduction Flux

The concluding part of the long-term carbon cycle in this model is the subduction flux. Unlike other atmospheric gases, CO_2 reacts with water to form carbonic acid rain, dissolving silicate rock through weathering. Carbon is then removed from the atmospheric system by chemical reaction of the dissolved CO_2 with Ca and Mg containing silicate minerals. This can be in the form of sediment as limestone ($CaCO_3$), or as organic matter (CH_2O), and is emplaced on the oceanic plates. The fate of 99% of the oceanic plates is to be subducted. Part of the carbon content on the plates will be accreted to the overriding plate, but it is estimated that this term is approximately balanced by the addition of carbon to the subducting plate, through tectonic erosion (Sleep & Zahnle 2001). At any time,

the amount of carbon R_p on the oceanic plates can be calculated by the mass balance equation,

$$\frac{dR_p}{dt} = \frac{F_w}{2} - F_{sub} + F_{sfw}. \quad (A8)$$

The weathering flux F_w as obtained by Equation (A2) is divided by 2 to account for the carbon that is rereleased to the atmosphere when the carbonates are formed. Then, the total amount of subducted carbon can be obtained by (Foley 2015)

$$F_{sub} = \frac{R_p L}{A_{plate}} v_p, \quad (A9)$$

where A_{plate} represents the area of the ocean plates. The area of the plates is retrieved by multiplying $(1 - l_f)$ by the surface area of a planet. The parameters v_p and L are the velocity of the plates and length of trenches, respectively.

It needs to be accounted for that not all of the subducted carbon will reach the deeper parts of the mantle, but instead that part of it will be reemitted into the atmosphere by arc volcanism. This is achieved by establishing the arc-volcanism flux F_{arc},

$$F_{arc} = f F_{sub}, \quad (A10)$$

where f is the fraction that degasses by arc volcanism. As of today, f is not well constrained, and estimates vary as much as 25%–70% (Foley 2015). Hence, an average value of 50% will be assumed since it does not affect the outcomes in significant ways.

Finally, the reservoirs need to be connected through the fluxes. The amount of carbon on oceanic plates was earlier established in Equation (A8), so the mantle and atmospheric reservoirs are left to be determined. The quantity of carbon in the atmosphere and oceans combined is given by the mass balance equation (Foley 2015),

$$\frac{dR_{atm}}{dt} = F_{deg} + F_{arc} - \frac{F_w}{2} - F_{sfw}, \quad (A11)$$

and the amount of carbon in the mantle at any given time is

$$\frac{dR_{man}}{dt} = (1 - f) F_{sub} - F_{deg}. \quad (A12)$$

Appendix B
Thermal Evolution Model

The spherically averaged mantle temperature $\langle T_m \rangle$ evolves as

$$\rho_m C_P V_m \frac{d \langle T_m \rangle}{dt} = -A_s q_s + A_c q_c + V_m Q(t), \quad (B1)$$

where ρ_m, C_P, and V_m are the mantle density, heat capacity, and volume, respectively; A_s and A_c are the surface area of the planet and the core, respectively; and q_s and q_c are the surface and core heat flux, respectively. For the heat production $Q_m(t)$ we assume Earth's relative mantle abundances of the main radiogenic heat producing elements K, U, and Th, as given by (Korenaga 2008)

$$Q_m(t) = Q_0 \sum_i q_i \exp \left\{ -\frac{\log(2)}{h_i} (t - 4.5) \right\}, \quad (B2)$$

where t is the time in Gyr, Q_0 is the total present-day heat production rate, and $q_1...q_4$ and $h_1...h_4$ are the relative present-

day heat production rates and half-life times of ^{238}U, ^{235}U, ^{232}Th, and ^{40}K as given in Korenaga (2008).

The mantle heat flux is given by

$$q_m = k \frac{(T_u - T_s)}{\delta_u}, \qquad (B3)$$

where T_u is the temperature at the base of the upper boundary layer (or lithosphere) and T_s is the surface temperature.

The core temperature evolution is calculated based on the assumption that there are negligible concentrations of K, U, and Th in the core and is given by

$$\rho_c C_{p,c} V_c \frac{dT_c}{dt} = -A_c q_c. \qquad (B4)$$

ORCID iDs

Amanda Kruijver ⓘ https://orcid.org/0000-0002-7442-3052
Dennis Höning ⓘ https://orcid.org/0000-0002-1190-4895
Wim van Westrenen ⓘ https://orcid.org/0000-0001-5828-8885

References

Abbot, D. S., Cowan, N. B., & Ciesla, F. J. 2012, ApJ, 756, 178
Agee, C. B. 1998, PEPI, 107, 63
Batalha, N. M., Rowe, J. F., Bryson, S. T., et al. 2013, ApJS, 204, 24
Bercovici, D., & Ricard, Y. 2014, Natur, 508, 513
Bond, J. C., O'Brien, D. P., & Lauretta, D. S. 2010, ApJ, 715, 1050
Brady, P. V., & Gíslason, S. R. 1997, GeCoA, 61, 965
Colbourn, G., Ridgwell, A., & Lenton, T. 2015, GBioC, 29, 583
Cowan, N. B., & Abbot, D. S. 2014, ApJ, 781, 27
Dorn, C., Noack, L., & Rozel, A. B. 2018, A&A, 614, A18
Feulner, G., & Kienert, H. 2014, E&PSL, 404, 200
Fiquet, G., Auzende, A., Siebert, J., et al. 2010, Sci, 329, 1516
Foley, B. J. 2015, ApJ, 812, 1
Foley, B. J., Bercovici, D., & Landuyt, W. 2012, E&PSL, 331, 281
Franck, S., Block, A., von Bloh, W., et al. 2000, P&SS, 48, 1099
Fulton, B. J., Petigura, E. A., Howard, A. W., et al. 2017, AJ, 154, 109
Gerya, T. 2014, GondR, 25, 442
Haqq-Misra, J., Kopparapu, R. K., Batalha, N. E., Harman, C. E., & Kasting, J. F. 2016, ApJ, 827, 120
Hirschmann, M. M. 2000, GGG, 1, 1042
Hirschmann, M. M. 2018, E&PSL, 502, 262
Hirschmann, M. M., Tenner, T., Aubaud, C., & Withers, A. C. 2009, PEPI, 176, 54
Höning, D. 2020, GGG, 21, e09105
Höning, D., Tosi, N., & Spohn, T. 2019, A&A, 627, A48
Isson, T. T., Planavsky, N. J., Coogan, L. A., et al. 2020, GBioC, 34, e06061
Kadoya, S., Krissansen-Totton, J., & Catling, D. C. 2020, GGG, 21, e08734
Kadoya, S., & Tajika, E. 2014, ApJ, 790, 107
Kadoya, S., & Tajika, E. 2015, ApJL, 815, L7
Kasting, J. F. 1989, GPC, 1, 83
Kasting, J. F., & Catling, D. 2003, ARA&A, 41, 429
Kite, E. S., Manga, M., & Gaidos, E. 2009, ApJ, 700, 1732
Kopparapu, R. K., Ramirez, R., Kasting, J. F., et al. 2013, ApJ, 765, 131
Korenaga, J. 2008, RvGeo, 46, RG2007
Krissansen-Totton, J., Arney, G. N., & Catling, D. C. 2018, PNAS, 115, 4105
Krissansen-Totton, J., & Catling, D. C. 2017, NatCo, 8, 15423
Lozovsky, M., Helled, R., Dorn, C., & Venturini, J. 2018, ApJ, 866, 49
Madhusudhan, N., Agúndez, M., Moses, J. I., & Hu, Y. 2016, SSRv, 205, 285
Marcy, G. W., Weiss, L. M., Petigura, E. A., et al. 2014, PNAS, 111, 12655
Mills, B., Lenton, T. M., & Watson, A. J. 2014, PNAS, 111, 9073
Mills, B. J. W., Krause, A. J., Scotese, C. R., et al. 2019, GondR, 67, 172
Miyagoshi, T., Tachinami, C., Kameyama, M., & Ogawa, M. 2013, ApJL, 780, L8
Moriarty, J., Madhusudhan, N., & Fischer, D. 2014, ApJ, 787, 81
Moynier, F., & Fegley, B. 2015, in The Early Earth: Accretion and Differentiation, ed. J. Badro & M. Walter, Vol. 212 (Hoboken, NJ: Wiley), 27
Næraa, T., Scherstén, A., Rosing, M., et al. 2012, Natur, 485, 627
Noack, L., & Breuer, D. 2014, P&SS, 98, 41
Noack, L., Rivoldini, A., & Van Hoolst, T. 2017, PEPI, 269, 40
Ohtani, E., Nagata, Y., Suzuki, A., & Kato, T. 1995, ChGeo, 120, 207
Oosterloo, M., Höning, D., Kamp, I., & Van Der Tak, F. 2021, A&A, 649, A15
Orcutt, B. N., Daniel, I., & Dasgupta, R. 2019, Deep Carbon: Past to Present (Cambridge: Cambridge Univ. Press) doi:10.1017/9781108677950
Papuc, A. M., & Davies, G. F. 2008, Icar, 195, 447
Ribas, I. 2009, in IAU Symp. 264, Solar and Stellar Variability: Impact on Earth and Planets (Cambridge: Cambridge Univ. Press), 3
Rushby, A. J., Johnson, M., Mills, B. J., Watson, A. J., & Claire, M. W. 2018, AsBio, 18, 469
Schaefer, L., & Sasselov, D. 2015, ApJ, 801, 1
Schubert, G., Turcotte, D. L., & Olson, P. 2001, Mantle Convection in the Earth and Planets (Cambridge: Cambridge Univ. Press) doi:10.1017/CBO9780511612879
Sleep, N. H., & Zahnle, K. 2001, JGR, 106, 1373
Stamenković, V., Breuer, D., & Spohn, T. 2011, Icar, 216, 572
Stamenković, V., Noack, L., Breuer, D., & Spohn, T. 2012, ApJ, 748, 41
Stixrude, L. 2014, RSPTA, 372, 20130076
Sundquist, E. T. 1991, QSRv, 10, 283
Tackley, P. J., Ammann, M., Brodholt, J. P., Dobson, D. P., & Valencia, D. 2013, Icar, 225, 50
Turcotte, D. L., & Schubert, G. 2002, Geodynamics (Cambridge: Cambridge Univ. Press) doi:10.1017/CBO9780511807442
Urey, H. C. 1952, PNAS, 38, 351
Valencia, D., O'Connell, R. J., & Sasselov, D. 2006, Icar, 181, 545
Valencia, D., O'Connell, R. J., & Sasselov, D. D. 2007, ApJL, 670, L45
Van den Berg, A. P., Yuen, D. A., Umemoto, K., Jacobs, M. H., & Wentzcovitch, R. M. 2019, Icar, 317, 412
Walker, J. C. G., Hays, P. B., & Kasting, J. F. 1981, JGR, 86, 9776
Warren, S. G., Brandt, R. E., Grenfell, T. C., & McKay, C. P. 2002, JGRC, 107, 3167
West, A. J., Galy, A., & Bickle, M. 2005, E&PSL, 235, 211
Ye, Q., Tong, J., Xiao, S., et al. 2015, Geo, 43, 507